

Doubled heterogeneous crystal nucleation in sediments of hard sphere binary-mass mixtures

Hartmut Löwen¹ and Elshad Allahyarov^{1,2,3,a)}

¹*Institut für Theoretische Physik, Heinrich-Heine-Universität Düsseldorf, D-40225 Düsseldorf, Germany*

²*Department of Physics, Case Western Reserve University, Cleveland, Ohio 44106, USA*

³*OIVTRAN, Joint Laboratory of Soft Matter, Moscow, 127412 Russia*

(Received 15 July 2011; accepted 13 September 2011; published online 6 October 2011)

Crystallization during the sedimentation process of a binary colloidal hard spheres mixture is explored by Brownian dynamics computer simulations. The two species are different in buoyant mass but have the same interaction diameter. Starting from a completely mixed system in a finite container, gravity is suddenly turned on, and the crystallization process in the sample is monitored. If the Peclet numbers of the two species are both not too large, crystalline layers are formed at the bottom of the cell. The composition of lighter particles in the sedimented crystal is non-monotonic in the altitude: it is first increasing, then decreasing, and then increasing again. If one Peclet number is large and the other is small, we observe the occurrence of a *doubled heterogeneous crystal nucleation* process. First, crystalline layers are formed at the bottom container wall which are separated from an amorphous sediment. At the amorphous-fluid interface, a secondary crystal nucleation of layers is identified. This doubled heterogeneous nucleation can be verified in real-space experiments on colloidal mixtures. © 2011 American Institute of Physics. [doi:10.1063/1.3646212]

I. INTRODUCTION

If a colloidal suspensions settles under strong gravity,¹ the bottom layers are typically crystalline.^{2–4} Gravity has, therefore, been used to grow large crystals, in particular on a patterned substrate^{5,6} which is used as a template for further crystallization. Much of recent attention has been devoted to study the crystallization process during sedimentation for hard spheres colloids, by experiments,^{7,8} density functional theory^{2,9} and computer simulation.^{2–4,10,11} Using confocal microscopy,^{12,13} it is possible to resolve the crystallization process on the particle scale, such that a detailed comparison between theory and experiment is feasible and the microscopic mechanism can be revealed.¹⁴

However, not much is known for the crystallization of colloidal mixtures under gravity. Sediments of binary charged mixtures are commonly used to determine the liquid-solid phase coexistence^{15–17} and the colloidal templating technique has recently also applied to colloidal mixtures.¹⁸ Recently, experiments on binary attractive colloids have revealed a wealth of crystallization and phase separation scenarios under gravity including novel zone formation.¹⁹ However, most of the theoretical^{20–24} and simulational^{25,26} studies for binary mixtures under gravity focus on a fluid sample.

Here, we study the crystallization of a binary mixture of hard spheres under gravity using Brownian dynamics computer simulations. The two species have the same diameter σ but differ in their buoyant masses ($m_1 < m_2$). Starting from a completely mixed system in a finite container, gravity is suddenly turned on, and the crystallization process in the sample is monitored. The strength of gravity is conveniently mea-

sured in terms of the Peclet numbers

$$Pe_\alpha = m_\alpha g \sigma / 2K_B T, \quad (1)$$

where $\alpha = 1, 2$, g denotes the gravity acceleration and $K_B T$ is the thermal energy. If both Peclet numbers are not too large, crystalline layers are formed at the bottom of the cell. As a result, we find that the composition of lighter particles in the sedimented crystal is non-monotonic in the altitude: it is first increasing, then decreasing and then increasing again, i.e., there is a marked *depletion zone* of light particles. If Pe_1 is large and Pe_2 is small, we observe the occurrence of a doubled heterogeneous crystal nucleation process. First, crystalline layers are formed at the bottom container wall which separated from an amorphous sediment. At the amorphous-fluid interface, a secondary crystal nucleation of layers is identified. This doubled heterogeneous nucleation can be verified in real-space experiments on colloidal mixtures either in gravity or in a centrifuge or under light pressure.²⁷ Our results may also be of relevance for granulates²⁸ and dusty plasmas.²⁹

This paper is organized as follows: we discuss the model and its equilibrium properties in Sec. II, including a brief discussion of the special case of equal masses. Then, we present extensive results of our computer simulations relevant for three different regimes of Peclet numbers in Secs. III–V. Finally, we conclude in Sec. VI.

II. MODEL AND SIMULATION TECHNIQUES

A. The model

We consider the simplest nontrivial binary mixture, namely, an equimolar mixture of hard spheres with the same diameters but different masses. The advantage of this choice

^{a)}Electronic mail: elshad.allahyarov@case.edu.

is that the equilibrium phases at vanishing gravity coincides with that of the simple hard sphere system. The latter is known and simple,³⁰ in contrast to hard sphere mixtures with different sizes where the equilibrium phase diagram is complex.³¹ Nevertheless, under the action of gravity, there are nontrivial compositional effects in our model due to the different buoyant masses.

We consider a rectangular simulation box with dimensions L_x , L_y , and L_z containing $N/2$ heavy particles with mass m_2 and $N/2$ light particles with mass m_1 . We denote the mass ratio as $\gamma = m_2/m_1 > 1$. The system is started from an initial homogeneously mixed fluid configuration of volume fraction $\Phi_0 = \frac{\pi\sigma^3}{6} \frac{N}{L_x L_y L_z}$. The packing parameter Φ_0 and the length of the box L_z define the areal density of particles (the number of particles per area of the orthogonal xy -plane)

$$\eta_A = N\sigma^2/L_x L_y = \Phi_0 \frac{6L_z}{\pi\sigma}. \quad (2)$$

There is a hard wall at the bottom of the sample at $z = 0$. Brownian dynamics is assumed to model the completely overdamped colloidal motion. Both species have the same friction constant, respectively to the same short-time diffusion coefficient D_0 .

B. Equilibrium phase diagram and equilibrium density profiles

Let us start with the equilibrium behaviour as a reference. First of all, for vanishing gravity ($g = 0$), the *bulk equilibrium phase diagram* is very closely related to that of a pure (mono-mass) hard sphere system, since the interaction and, therefore, the excess free energy are not affected by the second species. Hard spheres are athermal, hence temperature is just a trivial energy scaling such that the phase diagram of the mixture only depends on two variables which can conveniently be chosen as two chemical potentials μ_1 and μ_2 . A mono-mass system with indistinguishable spheres corresponds to $\mu_1 = \mu_2$ (diagonal line in Figure 1). At the chemical potential μ_c of fluid-crystal coexistence, there is first-order phase transition from a fluid into an fcc-crystal.³² Note that the equality of the two chemical potentials can also be interpreted as an equimolar mixture which constitutes the starting configuration of our simulations. Different chemical potentials imply different partial densities, i.e., compositions of the mixture different from 50%. Since the hard sphere bulk freezing does not depend on the labelling (or coloring) of particle species, there is a similar fluid-to-crystal transition away from the $\mu_1 = \mu_2$ diagonal. The full coexistence is sketched as a dashed (red) line in Figure 1 which separates a fluid mixture from a randomly occupied fcc crystal. Along the coexistence line, the composition changes without affecting the total density.

Now we turn to a discussion of the equilibrium (coarse-grained) partial density profiles *in gravity* ($g > 0$). For weak gravity, far enough away from the bottom wall, it is known that raising the altitude z in a sediment corresponds exactly to a linear path in the $\mu_1\mu_2$ -plane²³ the slope of which is given by the mass ratio γ and the offset can be controlled by the initial bulk chemical potentials. This can be readily derived from density functional theory in the grand-canonical ensemble. At

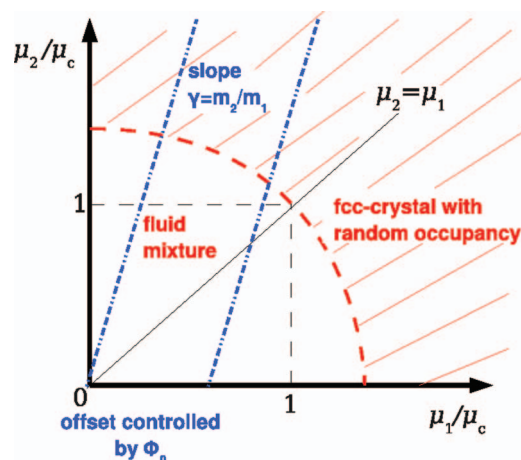


FIG. 1. Schematic representation of the equilibrium bulk phase diagram of the binary hard sphere mixture in the plane spanned by the two chemical potentials μ_1 and μ_2 which are both scaled by the coexistence chemical potential of the pure hard sphere freezing point μ_c . Separated by a coexistence line (red dashed line), there is a stable fluid mixture and a randomly occupied fcc-crystal. Changing altitude in a sediment corresponds to a linear path in this diagram with slope γ (blue dotted-dashed line). The offset of this path can be controlled by Φ_0 .

given altitude z , the system is locally mapped onto a bulk system with effective chemical potentials $\mu_1 = \mu_1^0 - m_1 g z$ and $\mu_2 = \mu_2^0 - m_2 g z$. Here, μ_1^0 and μ_2^0 are the overall chemical potentials imposed for the gravitational system which determine the overall partial densities. Eliminating z yields a linear relation between μ_1 and μ_2 , namely, $\mu_2 = \gamma\mu_1 + \mu_2^0 - \gamma\mu_1^0$ with a slope γ and an offset $\mu_2^0 - \gamma\mu_1^0$. Proceeding in altitude is, therefore, equivalent to following the dashed-dotted (blue) line downwards in Figure 1. At the point where this line intersects the coexistence line, there is change in phase in the sediment from a crystal to a fluid. It is also important to note that along the linear path, both the total density and the relative composition of the heavy particles decrease monotonically in the height. Therefore, any increase in total density and any increase in composition of heavy particles contradict equilibrium principles. We strongly expect that these general features persist for arbitrary gravitational strength $g > 0$.

C. Non-equilibrium crystallization in a one-component (mono-mass) system under gravity

For $\gamma = 1$, we recover the special case of a one-component (mono-mass) system which was studied previously¹¹ using similar simulation techniques as applied here. Let us summarize the main results regarding the crystallization behaviour for the one-component hard sphere system. An initial homogeneous starting configuration of total height L_z and volume fraction Φ_0 was used with a hard bottom wall. A threshold value for the Peclet number Pe_c was found below which the system crystallizes almost completely. If the actual Peclet number is above Pe_c , the crystallization process is overtaken by the formation of an amorphous block such that the resulting phase sequence in the sediment is crystal/amorphous/fluid. The critical value Pe_c depends

strongly on the initial volume fraction Φ_0 but is only weakly depending on the areal density η_A . For $\Phi_0 = 0.1$, $Pe_c \approx 2$, and for $\Phi_0 = 0.3$, $Pe_c \approx 1$. This behaviour was explained by a splitting of the crystalline-amorphous interface from the amorphous-liquid interface.

The crucial point from the one-component system is, therefore, the existence of a critical Peclet number Pe_c . Thus, for a mass-binary system one should distinguish among the following regimes:

Regime I: Both loads, Pe_1 and Pe_2 , are smaller than Pe_c .

Regime II: $Pe_1 < Pe_c$, whereas $Pe_2 > Pe_c$.

Regime III: Both loads, Pe_1 and Pe_2 , are larger than Pe_c .

We consider all these regimes explicitly in this paper.

D. Simulation and analysis

Following our previous work,¹¹ we use an adapted code for hard spheres³³ of diameter σ in our Brownian dynamics computer simulations, where the short-time infinite-dilution diffusion coefficient D_0 sets the Brownian time scale $\tau_B = \sigma^2/D_0$. A small time step of $\Delta t = 0.001\tau_B$ was used in integrating the stochastic equations of motion. The simulation box contains 40 000 heavy and 40 000 light hard spheres and has a rectangular shape with dimensions $L_x = 40.8\sigma$, $L_y = 43.2\sigma$, and L_z varied between 80σ and 240σ . Based on studies with a halved cross section of the simulation box, lateral system size effects are expected to be small. Several systems with a packing fraction Φ_0 in the range $0.1 \leq \Phi_0 \leq 0.3$ were explored. Simulations were carried out for $\eta_A = 45.4$ chosen large enough to produce a crystal-fluid interface at a given gravitational strength Pe . The gravity acceleration g points along the $-z$ -direction. Periodic boundary conditions are employed in the x and y directions, while two hard walls are placed at $z = 0$ and $z = L_z$. Next to the wall at $z = 0$, we place a triangular layer of fixed spheres with a lattice constant $a = 1.133\sigma$ which acts as an initial template for crystal growth.³⁴ Without a template the crystallization happens in a few bottom layers containing small grains, large defects, and fault stackings. This strongly suppresses the formation and following upward propagation of a single-phase crystalline front along the sediment.

All simulations were started from an initial configuration with a homogeneous mixed distribution of colloids in the simulation box except the template particles in the seed layer next to the bottom wall. This mimics an initially stirred solution to which gravity is applied instantaneously.¹³ A total simulation time of $500\tau_B$ was accessed during our simulations. We averaged our results over 20 different initial configurations in order to improve the statistics.

For subsequent times t , we calculated the laterally averaged one-particle partial packing fractions as

$$\phi_\alpha(z, t) = \frac{\pi}{6} \frac{\sigma^3}{L_x L_y} \iint dx dy \rho_\alpha(x, y, z, t), \quad (3)$$

where $\alpha = 1, 2$, and $\rho_\alpha(x, y, z, t)$ is the local one-body partial density of particles at a given time t . Clearly, the total packing fraction is $\phi(z, t) = \phi_1(z, t) + \phi_2(z, t)$.

We further identified ‘‘crystalline’’ particles with a crystal-like surrounding according to a commonly used criterion:³⁵ the local orientational-order parameter $\bar{q}_6(i)$ is calculated for each particle i .^{36,37} When two particles i and j are separated by $r \leq 1.3\sigma$, we associate a crystalline bond to these particles, if $\bar{q}_6(i) \cdot \bar{q}_6(j) > 0.5$. A particle which has at least 8 of these bonds is considered to be crystalline. All other particles are identified as ‘‘liquid-like’’ particles. The corresponding local packing fractions of crystalline particles $n_c(z, t)$ and liquid particles $n_l(z, t)$ are also calculated and give rise to a q_6 interface. We define the *interface position* $z_0(t)$ by the implicit condition $n_c(z_0(t), t) = n_l(z_0(t), t)$, i.e., by the position where the fraction of crystalline particles equals that of the liquid-like particles. Accordingly, the *propagation velocity* of the solid-fluid interface is defined as $v(t) = dz_0(t)/dt$.

III. RESULTS FOR REGIME I

In regime I ($Pe_1 < Pe_c$, $Pe_2 < Pe_c$), we expect that a compositionally disordered crystal will nucleate and grow without entering into an amorphous glassy phase. However, what is *a priori* not clear is the change in composition as a function of height z and time t . Simulation data for the partial density profiles at the final time $t = 500\tau_B$ are shown in Figure 2 for five different mass ratios γ ranging between 1 and 4. The mono-mass system where $\gamma = 1$ is given as a reference case (a). The local packing fractions of crystalline and liquid particles, $n_c(z)$ and $n_l(z)$, are also shown. The open squares denote the maximal height where the two partial density profiles of the heavy and light particles intersect each other $\phi_1(z) = \phi_2(z)$. Clearly this height decreases with increasing γ at fixed $Pe_1 = 0.5$. This matching point of the light and heavy particles is in the liquid phase at lower γ , whereas it is in the crystalline phase at higher γ . Strong peaks in the laterally averaged density profile indicate crystalline order which is a bit smeared due to defects and misorientations of the planes. A clearer indication for crystallinity is contained in profiles of $n_c(z)$ and $n_l(z)$. $n_l(z)$ is almost zero where peaks occur indicating that all particles in layers are crystalline. The q_6 -interface is clearly visible as the intersection point of $n_c(z)$ and $n_l(z)$. In Figure 2(b) the profiles are similar to the mono-mass case shown in Figure 2(a). Apart from a small dip, the composition of light particles increases with altitude z (see the open circles in Figure 2(b)) which is the expected equilibrium trend. The dip becomes, however, much more pronounced for larger γ where a sharp drop to zero composition of light particles below the crystal-fluid interface is visible and a striking non-monotonic compositional behaviour shows up in Figures 2(d) and 2(e). This depletion zone of light particles below the q_6 -interface clearly contrasts equilibrium behaviour and, therefore, deserves more detailed analysis.

Before discussing the non-monotonic behaviour in more detail, we remark that the average distance between crystalline layers shrinks as a function of Pe_2 : there were

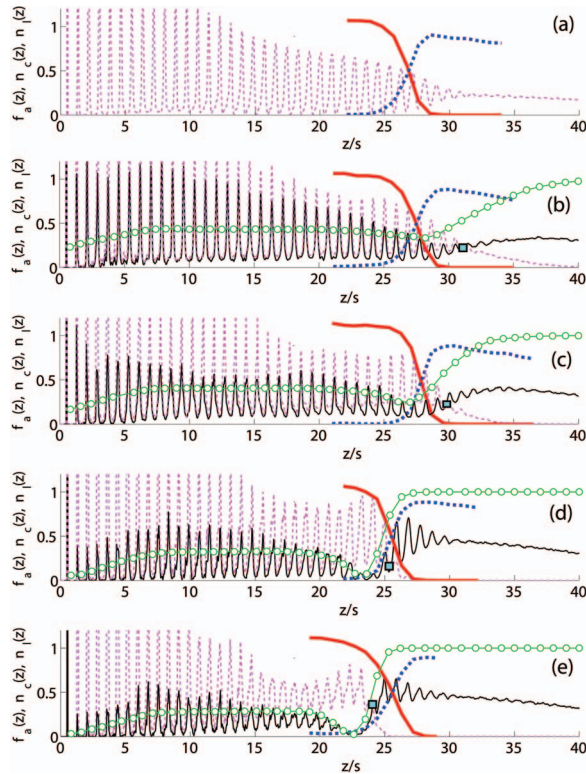


FIG. 2. (a)–(e) Simulation results for laterally averaged packing fractions $\phi_\alpha(z)$ for $Pe_1=0.5$ and $\Phi_0=0.1$ at $t=500\tau_B$. $\alpha=1, 2$ for the light and heavy particles correspondingly. From top to bottom, the parameter $\gamma = m_2/m_1 = Pe_2/Pe_1$ is changed as 1, 1.5, 2, 3, and 4. Thin full line: light particles $\phi_1(z)$; thin dashed line (pink in online version): heavy particles $\phi_2(z)$; thick full line (red in online): interfacial profile $n_c(z)$ for the “crystalline” particles; thick dashed line (blue in online): interfacial profile $n_l(z)$ for the “liquid-like” particles. Open squares denote the matching point where the partial densities of heavy and light particles intersect. Line with open circles: the composition of the light particles along the sediment.

24 layers within $0 < z < 20\sigma$ at $Pe_2 = 0.5$, whereas there are 25 layers within the same range at $Pe_2 = 2$ (see Figure 2). This has to do with the obvious fact that stronger gravity compresses the crystalline layers more.

Figure 3 shows the time evolution of the density profiles at the largest mass ratio $\gamma = 4$, where the composition behaves anomalously. The following picture emerges: when the sedimentation starts from a homogeneously mixed state at a fluid volume fraction Φ_0 , heavy particles tend to sediment faster to the bottom. They form the first crystalline layers at the bottom and exclude the lighter particles due to buoyancy. Therefore, the first few layers are mainly composed of heavy particles. When the light particles effectively float up, crystallization occurs which arrests them into cages where they remain frozen on the time scale of the simulation. This explains the increase in composition of the crystalline sediment with lighter particles. Further upwards in altitude, the crystallization front becomes slower and this gives the lighter particles the chance to float up more. Thereby light particles are replaced by heavy particles in the front of the slowly advancing crystal-liquid interface. There is even a formation of a few pure crystalline layers of heavy particles completely free from light particles. Further upwards in altitude, on the other hand, there are crystalline regions made by light particles alone.

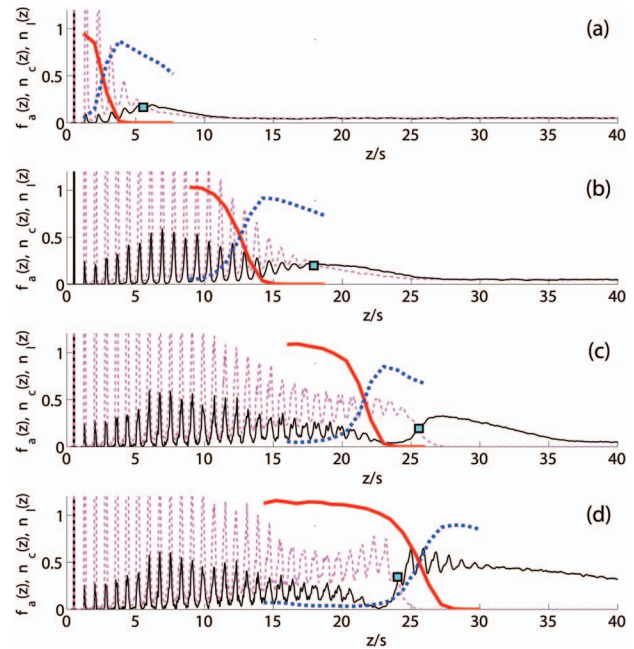


FIG. 3. (a)–(d) Simulation results for laterally averaged packing fractions $\phi_\alpha(z)$ for $Pe_1=0.5$, $Pe_2=2$, $\Phi_0=0.1$, and $\gamma=4$ for different simulation times. $\alpha=1, 2$ for the light and heavy particles correspondingly. From top to bottom: $t=10\tau_B, 40\tau_B, 70\tau_B, 250\tau_B$. Thin full line: light particles $\phi_1(z)$; thin dashed line (pink in online version): heavy particles $\phi_2(z)$; thick full line (red in online): interfacial profile $n_c(z)$ for the “crystalline” particles; thick dashed line (blue in online): interfacial profile $n_l(z)$ for the “liquid-like” particles. Open squares denote the matching point where the partial densities of heavy and light particles intersect.

Concomitantly, the matching point (open squares in Figure 2), where the partial densities of heavy and light particles intersect, behaves non-monotonic in time, it first moves up and then comes down again, in line with the exchange of heavy and light particles. More details of this exchange process at the slowly growing crystallization front are shown in Figures 4 and 5. Figure 4 shows no depletion of light particles at $t=50\tau_B$ but the inverse at $t=100\tau_B$. Figure 5 indicates that the number of light particles up to a height of $z=24$ (marking approximately the end of the depletion zone) behaves non-monotonic in time, see also the inset in Figure 5. This shows that the light particles are taken away from the depletion zone and are levitated to the upper layers of suspension due to the incoming mass of heavy particles. The depletion zone stops to develop once the interface passes through it, and the crystallization of the excess heavy particles freezes-in the whole structure.

The interface position $z_0(t)$ and its propagation speed $v(t)$ are shown in Figure 6. A comparison to the corresponding

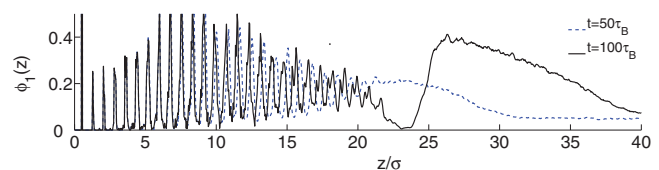


FIG. 4. Simulation results for density profiles of light particles $\phi_1(z)$ for $Pe_1=0.5$, $Pe_2=2$, $\Phi_0=0.1$, and $\gamma=4$ at two different simulation times $t=50\tau_B$ (dashed line) and $t=100\tau_B$ (full line).

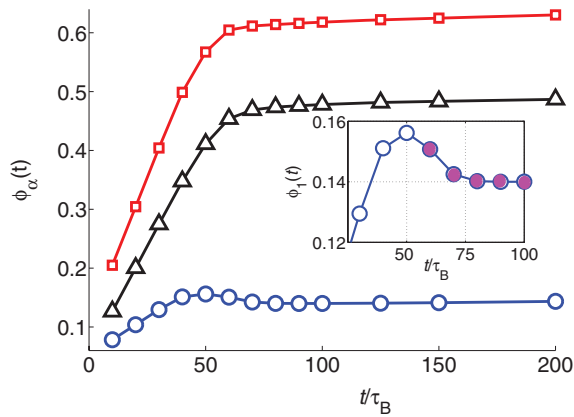


FIG. 5. Average packing fraction of particles in the area $0 < z < 24\sigma$ of the sediment where a levitation of light particles takes place. Simulation parameters are $Pe_1 = 0.5$, $Pe_2 = 2$, $\Phi_0 = 0.1$, and $\gamma = 4$. Line with square (red in online): total packing fraction; line with triangles (black in online): heavy particles; line with circles (blue in online): light particles. The inset shows in detail the nonlinear behaviour of light particle packing fraction $\phi_l(t)$ for $25\tau_B < t < 100\tau_B$. Filled circles in the inset correspond to simulation times at which a depletion zone in light particle densities develops.

results of a mono-mass system both for $Pe = Pe_1 = 0.5$ and $Pe = Pe_2 = 2$ reveals that the dynamics of the binary-mass system is mostly determined by the motion of the heavy particles. As expected, the formation of the depletion zone of light particles correlates with the drop of the interfacial velocity $v(t)$ at time $t/\tau_B \approx 70$, thus giving lighter particles more time to float up before their freezing process occurs.

In conclusion, we have shown that the compositional effects in a growing binary crystal front is highly nontrivial. A growing crystal-fluid interface freezes-in the structures. If this interface slows down, the separation process between heavy and light particles is getting time to develop and forms a depletion zone of light particles contrasting the monotonic behaviour in equilibrium profiles.

IV. RESULTS FOR REGIME II

In regime II ($Pe_1 < Pe_c$, $Pe_2 > Pe_c$), the corresponding mono-mass system forms an amorphous sediment on top of few crystalline bottom layers. We still keep the lighter species away from this regime, i.e., $Pe_1 < Pe_c$. Let us first discuss results for a special parameter selection, namely, $Pe_1 = 0.7$, $Pe_2 = 1.4$ at $\Phi_0 = 0.3$. For $\Phi_0 = 0.3$, $Pe_c \approx 1$, and thus, both conditions $Pe_1 < Pe_c$ and $Pe_2 > Pe_c$ are fulfilled. Other parameter combinations are considered later.

Figure 7 shows the time evolution of the partial density profiles. First, heterogeneous nucleation occurs at the patterned bottom wall similar as found in regime I. Then, after the formation of about 12 crystalline layers, an amorphous sediment is built, as clearly signalled by the high number of liquid-like particles and the simultaneous loss of crystal-like particles. The crystalline-amorphous interface gets quickly stuck in time but the amorphous-fluid interface is still growing. The latter is defined by the intersection point of the total packing fraction profile with the freezing packing fraction 0.492 (Ref. 38) and is indicated by a vertical arrow in Figure 7. At larger times, the amorphous-fluid interface stops

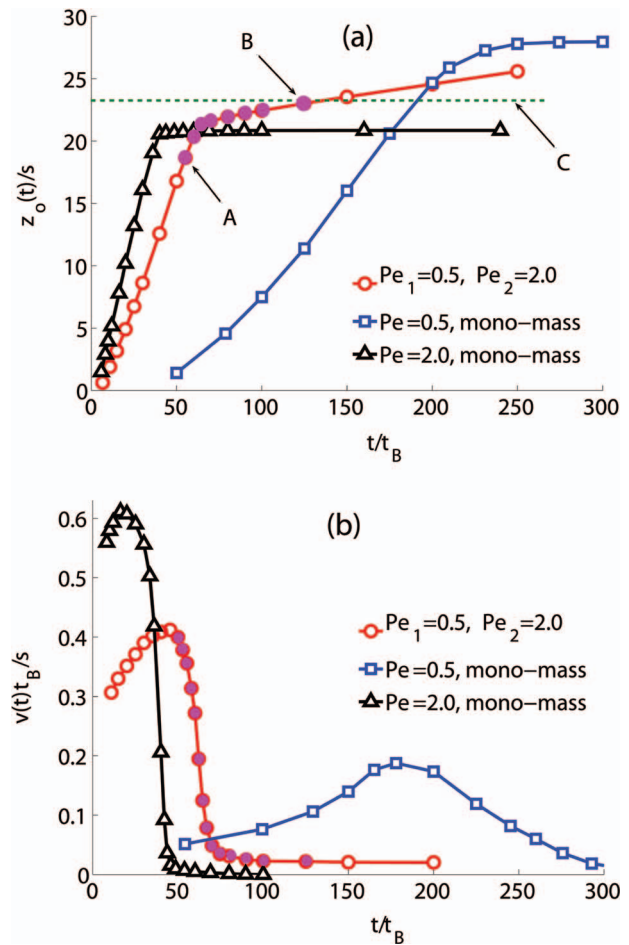


FIG. 6. Reduced interface position $z_0(t)/\sigma$ (a) and reduced propagation velocity $v(t)\tau_B/\sigma$ (b) as functions of simulation time t/τ_B . Line with circles (red in online): binary mass system with $Pe_1 = 0.5$, $Pe_2 = 2$, $\Phi_0 = 0.1$, and $\gamma = 4$. Line with triangles (black in online): mono-mass system with $Pe = 0.5$, and $\Phi_0 = 0.1$. Line with squares (blue in online): mono-mass system with $Pe = 2$, and $\Phi_0 = 0.1$. In (a), the dashed horizontal line C (green in online) corresponds to the distance at which a depletion zone in the local density of light particles $\phi_1(z)$ has a minimum. The arrows A and B in (a) point to the time window within which a depletion zone develops; see also filled circles in (a) and (b).

to grow, too, but slightly below its position a significant portion of crystal is emerging. This secondary heterogeneous nucleation at the amorphous-fluid interface is clearly signalled by the peak in the crystalline particles $n_c(z)$ at large times with a concomitant decrease in the liquid-like particles $n_l(z)$ (see the inset of Figure 7(a)). Though there is no clear lateral layering due to lattice misorientation with respect to the gravity normal such that there are no peaks in the partial density profiles, the peak in $n_c(z)$ unambiguously proves crystalline order. For the parameters shown in Figure 7, the emerging crystal is mainly composed of heavy particles. Therefore, we found a *doubled heterogeneous nucleation*: first it happens at the bottom wall and then below the amorphous-liquid interface.

The structure of the emerging secondary crystal is best shown in simulation snapshots. Figure 8(a) gives a snapshot at early time $t/\tau_B = 20$ of the crystallization process. Only the crystalline particles are shown. A formation of the first heterogeneous nucleation at the bottom wall and the

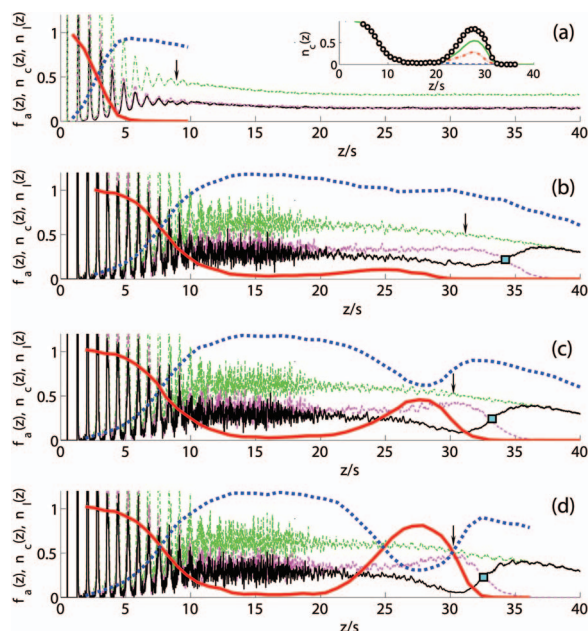


FIG. 7. (a)–(d) Simulation results for laterally averaged packing fractions $\phi_\alpha(z)$ for $Pe_1 = 0.7$, $Pe_2 = 1.4$, $\Phi_0 = 0.3$, and $\gamma = 2$ for different simulation times. $\alpha = 1, 2$ for the light and heavy particles correspondingly. From top to bottom: $t = 5\tau_B$, $40\tau_B$, $80\tau_B$, 160 . Thin full line: light particles $\phi_1(z)$; thin dashed line (pink in online version): heavy particles $\phi_2(z)$; dotted-dashed line (green in online): $\phi_1(z) + \phi_2(z)$; thick full line (red in online): interfacial profile $n_c(z)$ for the “crystalline” particles; thick dashed line (blue in online): interfacial profile $n_l(z)$ for the “liquid-like” particles. Open squares denotes the matching point where the partial densities of heavy and light particles intersect. The arrows denote the position of the amorphous glass-liquid interface. The inset in (a) shows the interfacial profile $n_c(z)$ for the “crystalline” particles for simulation times $t = 20\tau_B$ (dashed line, blue in online), $t = 60\tau_B$ (dotted-dashed line, red in online), $t = 100\tau_B$ (full line, green in online), and $t = 160\tau_B$ (line with circles).

roughness of the crystal-fluid interface (see Ref. 39 for a discussion in equilibrium) are visible. Figure 8(b) just shows the crystalline heavy particles alone which are preferentially lower than the crystalline light particles but exhibit the same qualitative behaviour as in Figure 8(a). The situation changes at larger times, a snapshot for $t/\tau_B = 160$ is presented in Figure 9. Again, only the crystalline particles are shown. The xyz side view in Figure 9(a) clearly reveals two separated crys-

talline parts of the sediment, the lower one stems from the first heterogeneous nucleation and the other originates from a secondary heterogeneous nucleation. The xz side view in Figure 9(b) also shows that the layering is much more developed in the lower crystalline part of the sediment. Various crystalline patches with different orientations become visible in the upper part of the crystalline sediment.

We now plot the interface position $z_0(t)$ and its propagation speed $v(t)$ in Figure 10. As in regime I, a comparison with the two pure (mono-mass) systems shows that the dynamics of the binary-mass system is dominated by the motion of heavy particles. The sharp drop in the q_6 interfacial velocity occurs much earlier (at $t/\tau_B \approx 10$) than the arrest of the amorphous-fluid interface (at $t/\tau_B \approx 200$).

Finally, we have made sure that the secondary heterogeneous nucleation occurs in a broad range of parameters by examining other parameter combinations. The results of the final partial density profiles are presented in Figures 11 and 12. Figure 11 shows density profiles at the same initial volume fraction $\Phi_0 = 0.3$ but for two further combinations of Peclet numbers with fixed mass ratio $\gamma = 2$. The same scenario of doubled crystalline nucleation occurs albeit the crystalline portion is getting smaller with increasing Peclet number. Also the amorphous-liquid interface shifts to larger heights. This implies that the higher the Peclet number the less fluctuations are close to the amorphous-fluid interface which favor heterogeneous crystal nucleation. Always the secondary crystal formed is mainly composed of heavier particles.

Figure 12 shows four further parameter combinations, now with fixed $\Phi_0 = 0.1$ and $\gamma = 4$. Again a secondary crystalline part is found. Here, it is composed almost exclusively by the light particles.

Concluding this section, we have found a doubled heterogeneous crystal nucleation. The secondary nucleation occurs close to the amorphous-fluid interface. Qualitatively, the occurrence of secondary crystallization can be understood in the limit of large mass disparity ($\gamma \gg 1$). Then, the dynamics of the two species is completely decoupled. First the first species nucleates at the bottom wall and forms a sharp crystalline sediment. Once sedimentation of the first species is finished, the

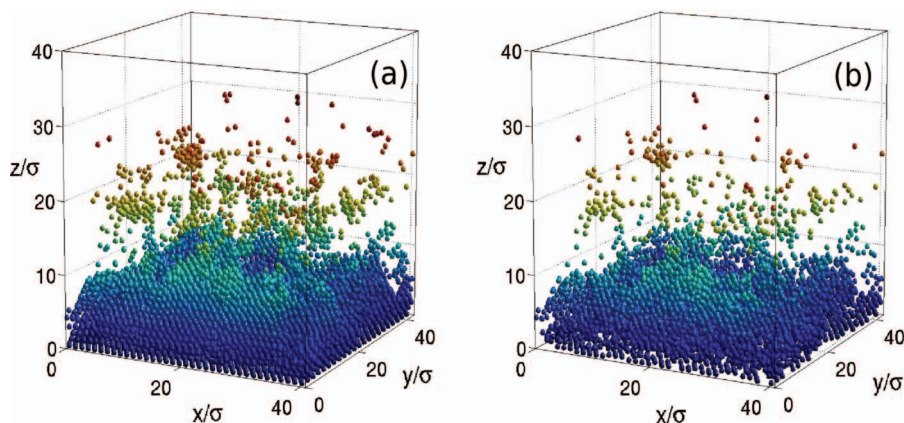


FIG. 8. 3D picture of simulation box for system parameters $Pe_1 = 0.7$, $Pe_2 = 1.4$, $\Phi_0 = 0.3$, $\gamma = 2$, $t = 20\tau_B$. Shown are all crystalline particles (a) and only the heavy crystalline particles with mass m_2 (b). Different particle shadings attribute to different particle altitudes: balls with darker shading (blue in online) are close, and balls with lighter shading (red in online) are the farthest away from the bottom of the box. Axis dimensions are given in particle diameter σ .

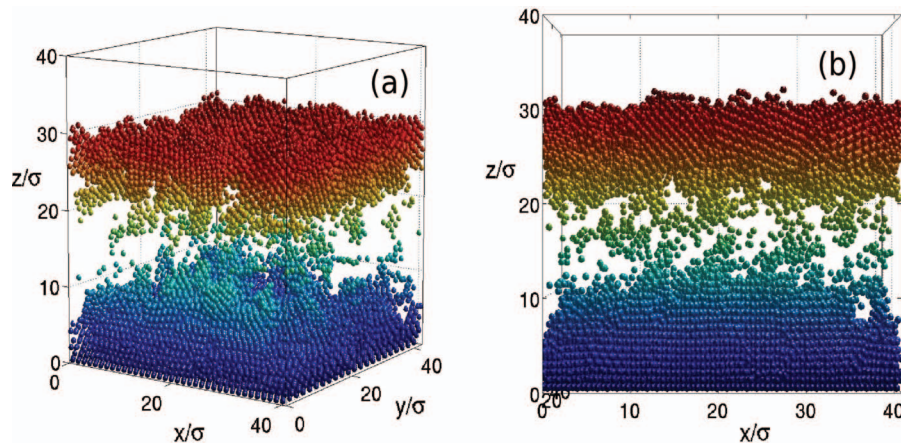


FIG. 9. The same as in Figure 8, but now for $t = 160\tau_B$. $Pe_1 = 0.7$, $Pe_2 = 1.4$, $\Phi_0 = 0.3$, $\gamma = 2$, $t = 160\tau_B$. Shown are all crystalline particles. (a) xyz side view and (b) xz side view.

light particles form their own crystalline sediment on top of the interface made by the heavy particles. Though this simple picture helps to explain secondary nucleation qualitatively, our simulation data show that even for small disparities, secondary nucleation is persistent. From this perspective it is also interesting that the secondary crystal for $\Phi = 0.3$ was mainly

composed of heavy particles different than in the simple picture above working at large disparities.

V. RESULTS FOR REGIME III

Regime III finally is defined by $Pe_1 > Pe_c$ and $Pe_2 > Pe_c$. Two examples for the resulting sediment in this regime are shown in Figure 13 for (a) $\Phi_0 = 0.3$, $\gamma = 2$, $Pe_1 = 2$, $Pe_2 = 4$, and (b) $\Phi_0 = 0.1$, $\gamma = 4$, $Pe_1 = 3$, $Pe_2 = 12$.

There is only a remnant of the secondary crystalline part indicated by a small maximum in the $n_c(z)$ -profile. The very strong gravity, thus, quickly freezes-in everything and only allows for a slight crystalline structure at the amorphous-fluid interface. The position of this crystalline remnant shifts to higher altitudes, if the Peclet numbers are increased. This

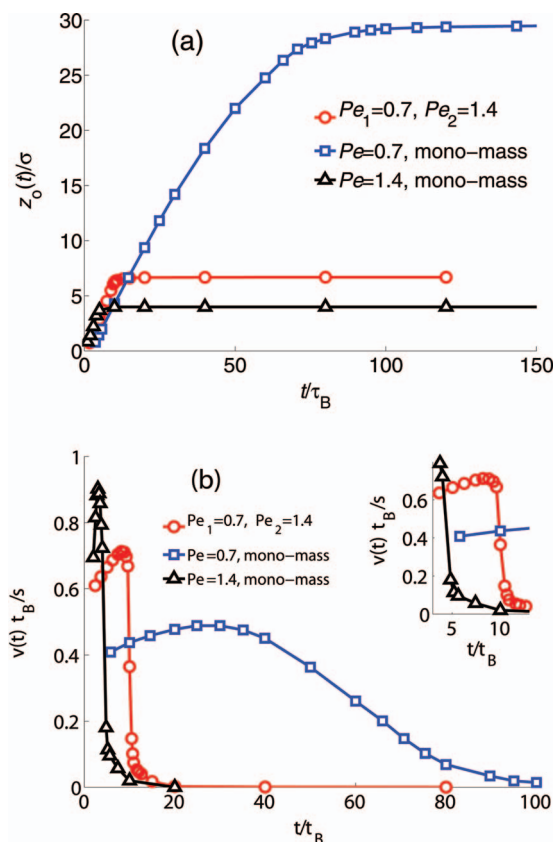


FIG. 10. Reduced interface position $z_0(t)/\sigma$ (a) and reduced propagation velocity $v(t)\tau_B/\sigma$ (b) as functions of simulation time t/τ_B . Line with circles (red in online): binary mass system with $Pe_1 = 0.7$, $Pe_2 = 1.4$, $\Phi_0 = 0.3$, and $\gamma = 2$. Line with triangles (black in online): mono-mass system with $Pe = 0.7$, $\Phi_0 = 0.3$. Line with squares (blue in online): mono-mass system with $Pe = 1.4$ and $\Phi_0 = 0.3$.

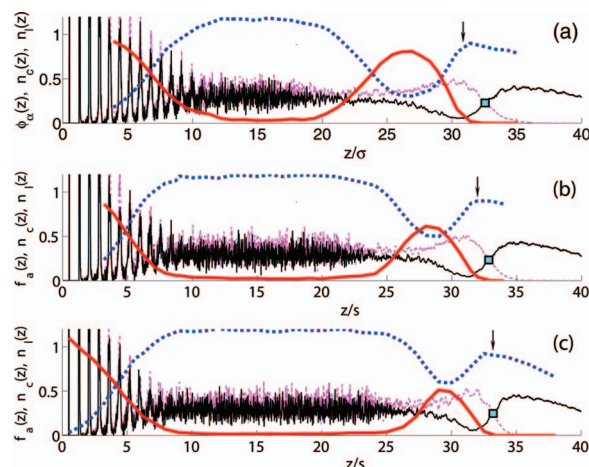


FIG. 11. Simulation results for laterally averaged packing fractions $\phi_\alpha(z)$ for $\Phi_0 = 0.3$, $\gamma = 2$ at $t = 500\tau_B$. $\alpha = 1, 2$ for the light and heavy particles correspondingly. From top to bottom: (a) $Pe_1 = 0.7$, $Pe_2 = 1.4$, (b) $Pe_1 = 0.9$, $Pe_2 = 1.8$, (c) $Pe_1 = 1.1$, $Pe_2 = 2.2$. Thin full line: light particles $\phi_1(z)$; thin dashed line (pink in online version): heavy particles $\phi_2(z)$; thick full line (red in online): interfacial profile $n_c(z)$ for the “crystalline” particles; thick dashed line (blue in online): interfacial profile $n_l(z)$ for the “liquid-like” particles. Open squares denote the matching point where the partial densities of heavy and light particles intersect. The arrows denote the position of the amorphous glass-liquid interface.

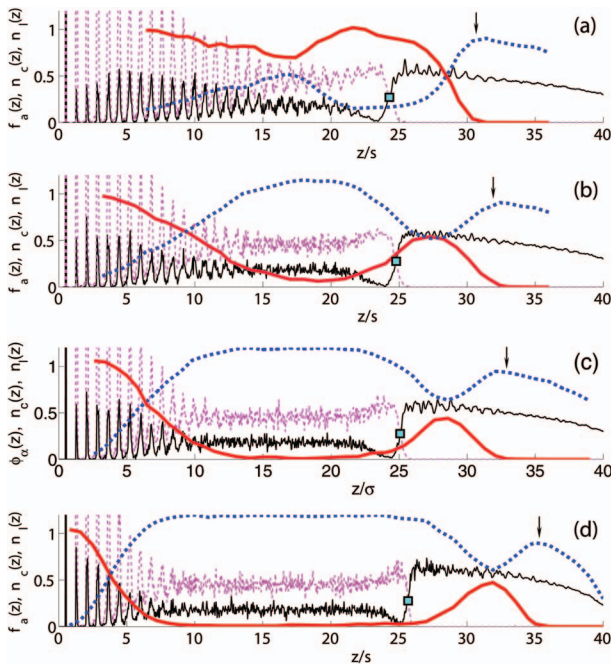


FIG. 12. Simulation results for laterally averaged packing fractions $\phi_\alpha(z)$ for $\Phi_0 = 0.1$, $\gamma = 4$ at $t = 500\tau_B$. $\alpha = 1, 2$ for the light and heavy particles correspondingly. From top to bottom: (a) $Pe_1 = 0.7$, $Pe_2 = 2.8$, (b) $Pe_1 = 0.9$, $Pe_2 = 3.6$, (c) $Pe_1 = 1.1$, $Pe_2 = 4.4$, (d) $Pe_1 = 1.8$, $Pe_2 = 7.2$. Thin full line: light particles $\phi_1(z)$; thin dashed line (pink in online version): heavy particles $\phi_2(z)$; thick full line (red in online): interfacial profile $n_c(z)$ for the “crystalline” particles; thick dashed line (blue in online): interfacial profile $n_l(z)$ for the “liquid-like” particles. Open squares denote the matching point where the partial densities of heavy and light particles intersect. The arrows denote the position of the amorphous glass-liquid interface.

trend becomes apparent when Figure 13(a) is compared to Figure 13(b). More importantly, in Figure 13(b), the larger relative difference in the two Peclet numbers leads to a stronger separation in light and heavy particles. This explains why the crystalline remnant shown in Figure 13(b) is completely composed of light particles.

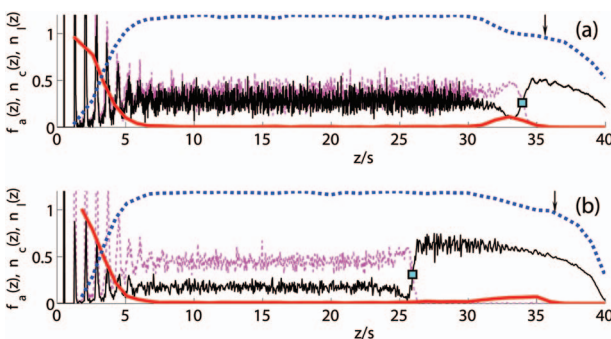


FIG. 13. Simulation results for laterally averaged packing fractions $\phi_\alpha(z)$ at $t = 500\tau_B$. $\alpha = 1, 2$ for the light and heavy particles correspondingly. (a) $\Phi_0 = 0.3$, $\gamma = 2$, $Pe_1 = 2$, $Pe_2 = 4$, (b) $\Phi_0 = 0.1$, $\gamma = 4$, $Pe_1 = 3$, $Pe_2 = 12$. Thin full line: light particles $\phi_1(z)$; thin dashed line (pink in online version): heavy particles $\phi_2(z)$; thick full line (red in online): interfacial profile $n_c(z)$ for the “crystalline” particles; thick dashed line (blue in online): interfacial profile $n_l(z)$ for the “liquid-like” particles. Open squares denote the matching point where the partial densities of heavy and light particles intersect. The arrows denote the position of the amorphous glass-liquid interface.

VI. CONCLUSION

In conclusion, we have explored the crystallization dynamics in a simple binary-mass hard sphere mixture during sedimentation from an initially homogeneously mixed sample. Extensive Brownian dynamics computer simulations were used to identify the crystalline part of the sediment and the corresponding interfaces between crystalline, amorphous, and fluid parts. The strength of gravity is characterized by the Peclet numbers of the two species Pe_1 and Pe_2 . If both Peclet numbers are smaller than the amorphization threshold Pe_c of the mono-mass system, there is a propagating crystal-fluid front but the composition of the lighter particle in the crystal is non-monotonic contradicting equilibrium properties. If one Peclet number is larger and the other is smaller than Pe_c , we observe a doubled heterogeneous crystal nucleation. The crystal first nucleates at the bottom of the sample and contains preferentially the heavy particles. Then, an amorphous sediment is formed above this crystal and finally on top of the amorphous sediment heterogeneous crystal nucleation occurs again. During this secondary crystallization process, a crystal is formed again which can contain both the heavy and light particles.

A doubled heterogeneous crystallization occurs also in other systems. One famous example is a peritectic grown from a mixture where first a phase A nucleates heterogeneously which is growing into the solution. On top of the emerging interface a second heterogeneous nucleation occurs for another B phase.⁴⁰ In this case, the interactions in the mixture are, however, more complicated and gravity is typically absent. Therefore, this does not exactly match our scenario of doubled heterogeneous crystal nucleation.

Our predictions are in principle verifiable in real-space experiment of sterically stabilized colloids.³⁵ Different buoyant masses can be obtained by using core-shell particles with different weights of the cores. The results have also relevance for binary granulates⁴¹ and dusty plasmas^{29,42} where similar real-space studies are possible. The crystallization in mass-bidisperse systems under gravity has recently also been explored for shaken granular matter (see Ref. 43).

Future investigations should address the following points: first of all, the hydrodynamic interactions mediated by the solvent should be taken into account explicitly in the computer simulation.^{44–46} Then, different hard sphere diameters should be considered, they will lead to much more complicated crystallites in the bulk,³¹ and it is expected that this will produce even more complex crystallization scenarios. Another variant of our model is one with negative masses. In a solvent, even the case $m_1 = -m_2 > 0$ could be realized. This model has received considerable attention for periodic boundary conditions in all three directions and is useful to detect laning of oppositely driven particles.^{47,48} The crystallization behaviour has also been explored⁴⁹ but not yet in a finite system with an impenetrable bottom wall. Third, long-ranged repulsive interactions (such as pair Yukawa interactions relevant for charged colloids⁵⁰) should be considered which lead to stable bcc bulk crystals. Fourth, a non-zero switching time for the onset of gravity should deserve future considerations. Next attractive interactions need more exploration in gravity

regarding their gelation and phase separation kinetics.¹⁹ Finally, the influence of different patterns at the bottom wall should be studied more regarding their effect on the growing crystalline structure.^{51,52}

ACKNOWLEDGMENTS

We thank M. Schmiedeberg, A. Härtel, and J. Horbach for helpful discussions. Financial support from the DFG within SPP 1296 is gratefully acknowledged. E.A. also acknowledges partial support of this work by the U.S. Department of Energy under Grant No. DE-FG02-05ER46244.

- ¹A. P. Philipse, *Curr. Opin. Colloid Interface Sci.* **2**, 200 (1997).
- ²T. Biben, R. Ohnesorge, and H. Löwen, *Europhys. Lett.* **28**, 665 (1994).
- ³M. Marechal and M. Dijkstra, *Phys. Rev. E* **75**, 061404 (2007).
- ⁴A. Mori, S. Yanagiya, Y. Suzuki, T. Sawada, and K. Ito, *J. Chem. Phys.* **124**, 174507 (2006).
- ⁵J. P. Hoogenboom, D. Derks, P. Vergeer, and A. van Blaaderen, *J. Chem. Phys.* **117**, 11320 (2002).
- ⁶I. B. Ramsteiner, K. E. Jensen, D. A. Weitz, and F. Spaepen, *Phys. Rev. E* **79**, 011403 (2009).
- ⁷R. Piazza, T. Bellini, and V. Degiorgio, *Phys. Rev. Lett.* **71**, 4267 (1993).
- ⁸R. P. A. Dullens, D. G. A. L. Aarts, and W. K. Kegel, *Phys. Rev. Lett.* **97**, 228301 (2006).
- ⁹T. Biben, J. P. Hansen, and J. L. Barrat, *J. Chem. Phys.* **98**, 7330 (1993).
- ¹⁰A. Mori, Y. Suzuki, and S. I. Yanagiya, *Fluid Phase Equilib.* **257**, 131 (2007).
- ¹¹E. Allahyarov and H. Löwen, *Europhys. Lett.* **95**, 38004 (2011).
- ¹²C. P. Royall, J. Dzubiella, M. Schmidt, and A. van Blaaderen, *Phys. Rev. Lett.* **98**, 188304 (2007).
- ¹³A. Wysocki, C. P. Royall, R. Winkler, G. Gompper, H. Tanaka, A. van Blaaderen, and H. Löwen, *Soft Matter* **5**, 1340 (2009).
- ¹⁴H. Löwen, *Soft Matter* **6**, 3133 (2010).
- ¹⁵N. J. Lorenz, H. J. Schöpe, and T. Palberg, *J. Chem. Phys.* **131**, 134501 (2009).
- ¹⁶T. Okubo, A. Tsuchida, S. Takahashi, K. Taguchi, and M. Ishikawa, *Colloid Polym. Sci.* **278**, 202 (2000).
- ¹⁷J. F. Gilchrist, A. T. Chan, E. R. Weeks, and J. A. Lewis, *Langmuir* **21**, 11040 (2005).
- ¹⁸E. C. M. Vermolen, A. Kuijk, L. C. Filion, M. Hermes, J. H. J. Thijssen, M. Dijkstra, and A. van Blaaderen, *Proc. Natl. Acad. Sci. U.S.A.* **106**, 16063 (2009).
- ¹⁹M. Leocmach, C. P. Royall, and H. Tanaka, *Europhys. Lett.* **89**, 38006 (2010).
- ²⁰T. Biben and J. P. Hansen, *Mol. Phys.* **80**, 853 (1993).
- ²¹H. S. Vesaratchanon, A. Nikolov, D. Wasan, and D. Henderson, *Ind. Eng. Chem. Res.* **48**, 6641 (2009).
- ²²X. L. Chu, A. D. Nikolov, and D. T. Wasan, *Chem. Eng. Commun.* **150**, 123 (1996).
- ²³M. Schmidt, M. Dijkstra, and J. P. Hansen, *Phys. Rev. Lett.* **93**, 088303 (2004).
- ²⁴M. Schmidt, M. Dijkstra, and J. P. Hansen, *J. Phys.: Condens. Matter* **16**, S4185 (2004).
- ²⁵A. Esztermann and H. Löwen, *Europhys. Lett.* **68**, 120 (2004).
- ²⁶J. Zwanikken and R. van Roij, *Europhys. Lett.* **71**, 480 (2005).
- ²⁷M. C. Jenkins and S. U. Egelhaaf, *J. Phys.: Condens. Matter* **20**, 404220 (2008).
- ²⁸E. Fried, M. E. Gurtin, and K. Hutter, *Continuum Mech. Thermodyn.* **16**, 199 (2004).
- ²⁹V. N. Tsyтович, G. Morfill, U. Konopka, and H. Thomas, *New J. Phys.* **5**, 66 (2003).
- ³⁰H. Löwen, *Phys. Rep.* **237**, 249 (1994).
- ³¹L. Filion and M. Dijkstra, *Phys. Rev. E* **79**, 046714 (2009).
- ³²M. Oettel, S. Görig, A. Härtel, H. Löwen, M. Radu, and T. Schilling, *Phys. Rev. E* **82**, 051404 (2010).
- ³³B. Cichocki and K. Hinsen, *Physica A* **166**, 473 (1990).
- ³⁴M. Heni and H. Löwen, *Phys. Rev. Lett.* **85**, 3668 (2000).
- ³⁵K. Sandomirski, E. Allahyarov, H. Löwen, and S. U. Egelhaaf, *Soft Matter* **7**, 8050 (2011).
- ³⁶P. J. Steinhart, D. R. Nelson, and M. Ronchetti, *Phys. Rev. B* **28**, 784 (1983).
- ³⁷P. R. ten Wolde, M. J. Ruiz-Montero, and D. Frenkel, *Phys. Rev. Lett.* **75**, 2714 (1995).
- ³⁸R. L. Davidchack and B. B. Laird, *J. Chem. Phys.* **108**, 9452 (1998).
- ³⁹T. Zykova-Timan, J. Horbach, and K. Binder, *J. Chem. Phys.* **133**, 014705 (2010).
- ⁴⁰H. Emmerich and R. Siquieri, *J. Phys.: Condens. Matter* **18**, 11121 (2006).
- ⁴¹J. A. Both and D. C. Hong, *Phys. Rev. E* **64**, 061105 (2001).
- ⁴²M. Rubin-Zuzic, G. E. Morfill, A. V. Ivlev, R. Pompl, B. A. Klumov, W. Bunk, H. M. Thomas, H. Rothermel, O. Havnes, and A. Fouqut, *Nat. Phys.* **2**, 181 (2006).
- ⁴³N. Rivas, S. Ponse, B. Gallet, D. Risso, R. Soto, P. Cordero, and N. Mujica, *Phys. Rev. Lett.* **106**, 088001 (2011).
- ⁴⁴A. Wysocki, C. P. Royall, R. Winkler, G. Gompper, H. Tanaka, A. van Blaaderen, and H. Löwen, *Faraday Discuss.* **144**, 245 (2010).
- ⁴⁵A. Wysocki, C. P. Royall, R. Winkler, G. Gompper, H. Tanaka, A. van Blaaderen, and H. Löwen, *Soft Matter* **5**, 1340 (2009).
- ⁴⁶A. Moncho-Jorda, A. A. Louis, and J. T. Padding, *Phys. Rev. Lett.* **104**, 068301 (2010).
- ⁴⁷J. Dzubiella, G. P. Hoffmann, and H. Löwen, *Phys. Rev. E* **65**, 021402 (2002).
- ⁴⁸T. Vissers, A. Wysocki, M. Rex, H. Löwen, C. P. Royall, A. Imhof, and A. van Blaaderen, *Soft Matter* **7**, 2352 (2011).
- ⁴⁹J. Dzubiella and H. Löwen, *J. Phys.: Condens. Matter* **14**, 9383 (2002).
- ⁵⁰H. Löwen and E. Allahyarov, *J. Phys.: Condens. Matter* **10**, 4147 (1998).
- ⁵¹M. Heni and H. Löwen, *Phys. Rev. Lett.* **85**, 3668 (2000).
- ⁵²L. Assoud, R. Messina, and H. Löwen, *Mol. Phys.* **109**, 1385 (2011).